Surface Wakes on Ultrasoft Solids

Aditi Chakrabarti,[1,*,†] Divya Jaganathan,[1,†] Robert Haussman,[1] and L. Mahadevan[1,2,‡]
[1]School of Engineering and Applied Sciences, Harvard University, Cambridge, Massachusetts 02138, USA
[2]Departments of Physics and Organismic and Evolutionary Biology, Harvard University, Cambridge, Massachusetts 02138, USA

(Received 10 November 2025; accepted 17 February 2026; published 2 April 2026)

We explore the dynamical response of the free surface of an ultrasoft solid driven by a localized moving pressure disturbance. Experiments reveal a steady V-shaped wake analogous to a surface Mach wedge. A simple geometric argument provides a qualitative explanation consistent with observations. A theoretical framework combining elastodynamic, capillary, and gravitational effects yields a generalized dispersion relation that smoothly interpolates between Kelvin's theory of liquid interface wakes and Rayleigh's theory of elastic surface waves. Our analysis explains the observed Mach-like behavior quantitatively while also emphasizing how elastodynamic effects can generate effective damping through radiative leakage. Together, our experiments and theory reveal the existence of a new regime that bridges fluid and solid surface-wave physics, offering new routes for probing the dynamics of soft interfaces.

DOI: 10.1103/lvvp-8pll

Soft elastic solids are easily deformable when subjected to external loads, and are characterized by relatively small (zero-frequency) shear moduli. The interface of a soft elastic solid is even softer than the bulk solid because in addition to a weak material response, it is soft by virtue of geometry (i.e., it is free on one side). Thus, soft interfaces are susceptible to both body forces (e.g., gravity [1]) and interfacial forces (e.g., surface tension [2]). For a solid with density ρ, elastic shear modulus μ, a surface energy per unit area γ, subject to a gravitational body force per unit volume ρg, one can define two natural length scales: an elastocapillary length, $\ell_{ce} = \gamma/\mu$ and an elastogravity length, $\ell_{eg} = \mu/\rho g$. For ultrasoft solids, elastic, capillary, and gravitational effects all become simultaneously important when the elastocapillary length and the elastogravity length become comparable. Then, letting $\ell_{eg} \sim \ell_{ce}$ yields an expression for the shear modulus $\mu^* \sim (\rho g \gamma)^{1/2}$; substituting $\rho = 1000$ kg/m^3, $g = 10m/s^2$, $\gamma = 100mN/m$ yields $\mu^* \sim 10Pa$. The recent ability to create very weak materials [3] with ultra-low moduli in this range, i.e., $\mu \sim O(10)Pa$ makes this capillary-gravity-elasticity regime accessible via tabletop experiments [4–7].

However, little is still known about the dynamics of ultrasoft solids, when there is a delicate interplay between inertia, elasticity, gravity, and capillarity, e.g., when a soft interface is driven by a transient pulse [8–11], a topic with implications for fields such as soft elastography [12,13] and nondestructive imaging [14,15]. Here, we study the two-dimensional wake left by a localized pressure source moving on the surface of a three-dimensional solid, using experiment and theory, while also linking together two classical problems: Rayleigh waves on the surface of an elastic solid [16] and the Kelvin wake behind a ship moving in deep water [17].

To create a dynamic pressure source moving at a speed U above a soft elastic solid [Fig. 1(a)], we start with a large tank filled with about 10 liters of an ultrasoft polyacrylamide hydrogel with elastic shear modulus, $\mu \approx 6.5$ Pa [see Supplemental Material (SM) Sec. A [18] for details of the protocol to create and measure the rheology of the gel] and density $\rho = 1000$ kg/m^3. The dimensions of the soft solid slab are 50 cm × 25 cm with a depth $H = 8$ cm. The pressure source was created by forcing compressed air out through a thin nozzle ($d = 0.84$ mm), mounted on a rail that can slide horizontally above the gel surface at a constant height of ∼4 cm above it. As the pressure source moves at a uniform speed (U) above the gel surface, we observe a wake behind the moving disturbance [Fig. 1(b), movies S2, S3, in SM [18]], with ridges of maximum surface elevation on the soft interface forming a linear wedgelike profile. The opening angle of the leading dominant ridge (2α) depends on the speed of the pressure source U; faster sources yield wakes with smaller angles. Indeed, plotting $\sin\alpha$ versus the scaled inverse speed of the pressure source c_s/U, where $c_s = \sqrt{\mu/\rho}$ is the shear-wave speed in the soft solid, we see a linear relationship with $\sin\alpha \approx 4.5 c_s/U$ [Fig. 1(c)].

A natural comparison of this observation is with the wake observed on liquid surfaces in the "deep-water" limit [17,22–25]. However, the wake angle here deviates substantially from the Kelvin angle (i.e., 19.4°) characteristic of gravity wakes at low source speeds in a few ways. First,

*Present address: Schlumberger-Doll Research, Cambridge, Massachusetts 02139, USA.
†These authors contributed equally to this work.
‡Contact author: lmahadev@g.harvard.edu

 © 2026 American Physical Society

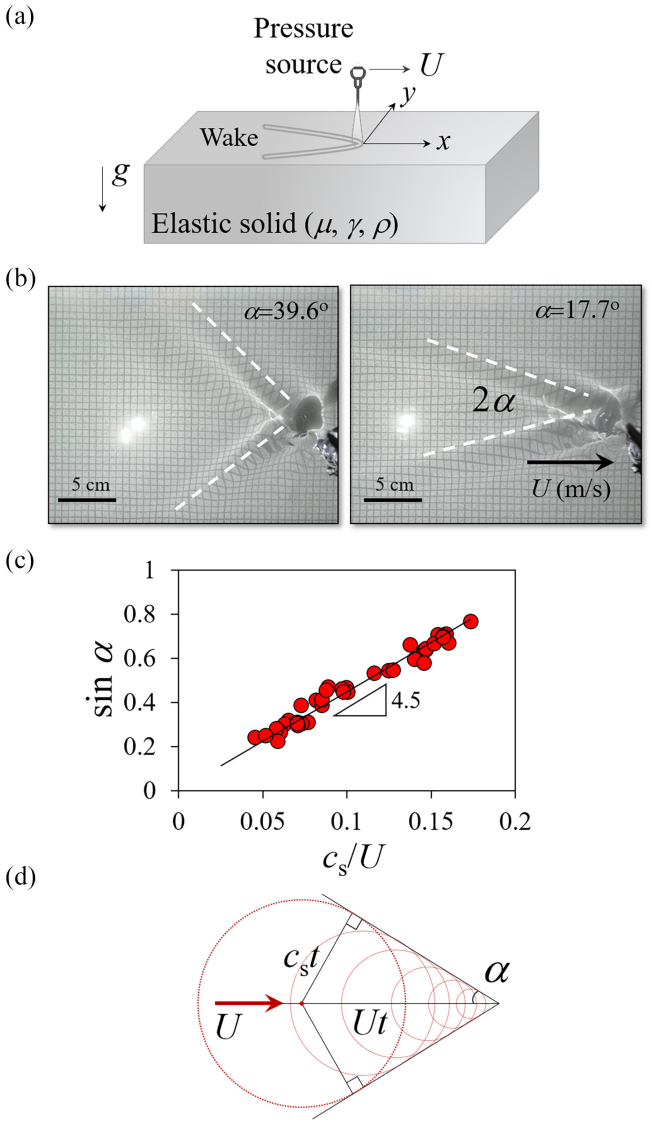

FIG. 1. (a) Schematic of the experimental setup, where a pressure source of compressed air moving at speed U impinges on the surface of an elastic solid, generating a surface wake. (b) Top-view images of wakes for two representative speeds, $U = 0.55\ m/s$ (left) and $U = 1.28\ m/s$ (right), leads to different opening angles (2α) on an ultrasoft solid ($\mu \approx 6.5\ Pa$). The wake angle decreases with the increasing speed of the pressure source. A projected grid on the surface of the gel slab from the top enables visualization of the surface deformation. (c) Experimental data showing Mach-like scaling, where $\sin\alpha$ varies linearly with c_s/U, and $c_s = \sqrt{\mu/\rho}$ is the Rayleigh (shear) wave speed. (d) Schematic of the geometry of wave fronts on a soft solid surface due to a moving pressure source in the ideal nondispersive Rayleigh limit.

the wake is sharper and more V-like without the feathered decorations seen in gravity waves. Second, the angle varies with the speed of the source without saturating to the Kelvin limit, like the classical gravity-capillary wakes with strong capillarity [26]. Finally, in contrast to gravity-capillary wakes, the wake patterns we observe exhibit only faint fine features away from the source, indicating strong damping (see SM [18] movie S1 for a comparison between soft gel and water wakes).

To get a qualitative understanding of our observations, we first consider a minimal model for the elastic wake, ignoring, in the first instance, the effects of gravity and capillarity. On the surface of an incompressible solid, freely propagating non-dispersive Rayleigh waves propagate with a speed proportional to the shear-wave speed c_s [16]. If a pressure source moves on the surface with a speed U greater than the c_s, we expect a Mach-like wake to emerge. A geometric argument for the wake half angle, α, follows by considering the superposition of the circular wave fronts [Fig. 1(d)] and leads to the simple relationship

$$\sin\alpha = Ac_s/U, \tag{1}$$

which is qualitatively consistent with our experimental measurements with $A \sim 4.5$, i.e., the wake angle increases with decreasing speed. To explain the weakly dispersive nature of the wake (see SM [18] movie S2), and the nonunity prefactor [27], we now turn to a quantitative theory of surface waves including the contributions from gravity, surface tension, and elastodynamics.

We assume that the free surface bounds a soft incompressible elastic half space ($z \leqslant 0$) of uniform density ρ and shear modulus μ. Displacements of the solid are given by $\boldsymbol{\xi}(\boldsymbol{x}, z, t) \equiv (\boldsymbol{u}, w)$, where $\boldsymbol{x} = (x, y)$. In the linear elastodynamic regime relevant for our observations, neglecting weak viscous effects (see SM Sec. B.4 [18] for justification), the dynamical equations of motion read,

$$\rho\frac{\partial^2\boldsymbol{\xi}}{\partial t^2} = -\boldsymbol{\nabla}P + \mu\nabla^2\boldsymbol{\xi}, \tag{2}$$

subject to the condition of incompressibility $\boldsymbol{\nabla}\cdot\boldsymbol{\xi} = 0$, which upon substituting into Eq. (2) gives

$$\nabla^2 P = 0. \tag{3}$$

Since we are interested in the response to small-amplitude disturbances at the surface, we take P to be the excess pressure from the prestressed equilibrium configuration, so that the boundary conditions deep in the interior are given by $\boldsymbol{\xi} \to \boldsymbol{0}$ and $P \to 0$ as $z \to -\infty$,. On the surface, capillary forces provide a stress proportional to the surface's mean curvature, yielding the free-surface boundary conditions $\sigma_{iz,0} = \mu(\partial w/\partial x_i + \partial u_i/\partial z)_{z=0} = 0, \sigma_{zz,0} = (-P + 2\mu\partial w/\partial z)_{z=0} = (P_z + \gamma\nabla_\parallel^2 w - \rho g w)_{z=0}$, where $i = x,\ y$ and $\boldsymbol{\nabla}_\parallel = (\partial/\partial x, \partial/\partial y)$, and $P_z(\boldsymbol{x}, t; U, L)$ is the disturbance field due to an external moving pressure source applied onto the surface, moving in the x direction with a constant speed U. For simplicity, we assume an isotropic pressure field with a characteristic size L.

We solve the linear Eqs. (2) and (3) subject to the boundary conditions using two-dimensional Fourier methods, assuming sufficient far-field decay, using the standard definition $f(\boldsymbol{x},z,t)=\int \mathrm{d}\omega \int[\mathrm{d}^2\boldsymbol{k}/(2\pi)^2]\tilde{f}(\boldsymbol{k},z,\omega)\mathrm{e}^{\mathrm{i}(\boldsymbol{k}\cdot\boldsymbol{x}-\omega t)}$, where $\tilde{f}$ is its corresponding transform, and the arbitrary function f can be P, $\boldsymbol{u}$, and w. This yields the complete solution (see SM Sec. B.2 [18] for details)

$$\tilde{P}=\frac{\omega^2(\omega^2-2c_s^2k^2)\mathrm{e}^{kz}}{D(k,\omega)}\tilde{P}_z(k,\omega), \tag{4}$$

$$\tilde{\boldsymbol{u}}=(\mathrm{i}\hat{\boldsymbol{k}})\frac{(\omega^2-2c_s^2k^2)k\mathrm{e}^{kz}+2(k^2c_s^2)q\mathrm{e}^{qz}}{\rho D(k,\omega)}\tilde{P}_z(k,\omega), \tag{5}$$

$$\tilde{w}=\frac{(\omega^2-2c_s^2k^2)k\mathrm{e}^{kz}+2(k^2c_s^2)k\mathrm{e}^{qz}}{\rho D(k,\omega)}\tilde{P}_z(k,\omega), \tag{6}$$

where $k=|\boldsymbol{k}|$, $q\coloneqq\sqrt{k^2-(\omega/c_s)^2}$, and the denominator

$$D(k,\omega)=\omega^2\left(gk+\frac{\gamma}{\rho}k^3\right)-(2c_s^2k^2-\omega^2)^2+4c_s^3k^3\sqrt{c_s^2k^2-\omega^2}, \tag{7}$$

which is consistent with the characteristic equation derived in [10] for the one-dimensional case.

For a disturbance pressure source moving with uniform velocity, as in our experiment, the Doppler shift sets $\omega=\boldsymbol{U}\cdot\boldsymbol{k}$. The stationary surface displacement field is then obtained from the Fourier transform of Eq. (6) evaluated at $z=0$ as follows [28,29]:

$$w(\boldsymbol{x})=\frac{1}{(2\pi)^2\rho}\int\int d^2\boldsymbol{k}e^{i\boldsymbol{k}\cdot\boldsymbol{x}}\frac{(\boldsymbol{U}\cdot\boldsymbol{k})^2k}{D(k,\boldsymbol{U}\cdot\boldsymbol{k})}\tilde{P}_z(k;L), \tag{8}$$

where $\boldsymbol{x}-\boldsymbol{U}t\to\boldsymbol{x}$, with $\boldsymbol{U}=U\boldsymbol{e}_x$, is the new coordinate vector in the moving frame. The stationarity condition,

$$\omega=\boldsymbol{U}\cdot\boldsymbol{k}=Uk\cos\phi, \tag{9}$$

where ϕ is the angle between the wave vector $\boldsymbol{k}$ and the direction of moving source [see Fig. 5(b)], restricts the surface waves that interfere constructively to those with phase speed $c_p(k)\coloneqq\omega/k<U$. Furthermore, the dispersion relation for surface waves is given by $D(k,\omega)=0$. We now examine the expression for D to understand the effects of elasticity.

To work with dimensionless quantities, we use the pressure source size L as the reference length and U/L as the reference frequency, and define $K\coloneqq kL$ and $\Omega\coloneqq\omega L/U$. This induces the transformation $(L^3/U^2g)D(K/L,\Omega U/L)\to D(K,\Omega)$, so that the dimensionless counterpart of Eq. (7) is

$$D(K,\Omega)=\Omega^2\Omega_{cg}^2-\mathrm{Fr}^2(2C_s^2K^2-\Omega^2)^2+4\mathrm{Fr}^2C_s^3K^3\sqrt{C_s^2K^2-\Omega^2}, \tag{10}$$

where $\Omega_{cg}^2\coloneqq K+\mathrm{Bo}^{-2}K^3$ is the dimensionless dispersion relation for gravity-capillary waves, $\mathrm{Bo}\coloneqq\sqrt{\rho gL^2/\gamma}=L/(\ell_{\mathrm{ce}}\ell_{\mathrm{eg}})^{1/2}$ is the Bond number, $\mathrm{Fr}=U/\sqrt{gL}$ is the Froude number, and $C_s\coloneqq c_s/U$ is the scaled shear-wave speed in the soft solid.

The dispersion relation for the soft surface, given by $D(K,\Omega)=0$, interpolates between two venerable classical problems involving surface waves [30]. When $C_s=0$, we recover the well-known dispersion relation for deep water dispersive gravity-capillary waves [23,31], with $\Omega=\Omega_{cg}/\mathrm{Fr}$. In the other limit, when $\Omega_{cg}=0(\mathrm{Fr}\to\infty)$, the dispersion relation satisfies $\Omega^2=2C_s^2K^2+2\sqrt{C_s^3K^3\sqrt{C_s^2K^2-\Omega^2}}$ [32] leading to the well-known theory of nondispersive Rayleigh waves on the surface of an incompressible half space with $\Omega\approx 0.955C_sK$ [16].

In our experiments, with $c_s\approx 0.08\ m/s$ and $U\in(0.5,1.4)\ m/s$, we have $C_s<0.2$. Assuming that the large-wave number contributions are suppressed by the finite bandwidth of the pressure source ($C_sK\ll 1$), the effects of elasticity may be treated perturbatively. This allows us to derive a dispersion relation that minimally captures the leading order effects due to elasticity, but unlike in the one-dimensional case [9,10], the two-dimensional problem warrants a distinction between modes as a function of the phase speeds ($C_p\coloneqq c_p/U$) relative to the shear-wave speed (C_s).

To facilitate discussion of these two different modes, we define a parameter $\lambda(K)\coloneqq C_s/C_p(K)$. Then, for modes propagating slower than the shear wave ($\lambda>1$), i.e., $C_p<C_s\ll 1$, the function D in Eq. (10) is real valued and reduces to

$$D(K,\Omega)=\Omega^2(\Omega_{cg}^2+4\varphi_1(\lambda^2)\mathrm{Fr}^2C_s^2K^2-\mathrm{Fr}^2\Omega^2), \tag{11}$$

where $\varphi_1\colon[1,\infty)\to[0,1/2)$ is a smooth bounded function (see SM Sec. B.3 [18]). We see that the softness of the elastic half space introduces a quadratic correction to the dispersion relation for classical gravity-capillary waves on a liquid half space. In contrast, for modes traveling faster than the shear wave ($\lambda<1$), i.e., $C_s<C_p<1$, the function D in Eq. (10) becomes complex valued and reduces to

$$D(K,\Omega)=\Omega^2(\Omega_{cg}^2+4\varphi_2(\lambda^2)\mathrm{Fr}^2C_s^2K^2-\mathrm{Fr}^2\Omega^2)+4i\Omega\mathrm{Fr}^2C_s^3K^3\sqrt{\varphi_2(\lambda^2)}, \tag{12}$$

where $\varphi_2\colon[0,1]\to[0,1]$ is yet another smooth bounded function (see SM B.3 [18]). Here, the softness introduces an additional leading-order cubic contribution to the

imaginary part of D, and the solution to $D(K,\Omega)=0$ lies in a small neighborhood of the solution to $\mathrm{Re}(D)=0$ in the complex $K-$ plane. The effective damping of the propagating surface waves even in the absence of any viscous effects in our energy-conserving theory is a consequence of bulk radiation that leads to leaky waves [9] that redistribute energy from the surface to the bulk.

For our experimental conditions, where the quantity $\mu/\sqrt{\rho g\gamma}=\sqrt{\ell_{\mathrm{eg}}/\ell_{\mathrm{ce}}}\sim 0.2$ is small, there are no real solutions to $D(K,\Omega)=0$ at the critical condition $\Omega=C_sK$, which precludes the simultaneous existence of fast and slow modes. Furthermore, we find that only the "leaky" fast modes are supported, because of the very low shear modulus of the ultrasoft gel [33] (see SM Sec. B.3 [18]). Henceforth, we consider only the reduced (real part of the) dispersion relation for fast modes from Eq. (12) to describe the wake pattern [34]:

$$\mathrm{Fr}\Omega=(K+\mathrm{Bo}^{-2}K^3+4\varphi_2(\lambda^2)\mathrm{Fr}^2C_s^2K^2)^{1/2}, \tag{13}$$

which yields a relation for the (square of the) dimensionless phase speed:

$$\mathrm{Fr}^2C_p^2=1/K+K/\mathrm{Bo}^2+4\varphi_2(\lambda^2)\mathrm{Fr}^2C_s^2. \tag{14}$$

This curve, plotted in Fig. 2, shows that the phase speed has a minimum at $K^*=\mathrm{Bo}$, with the corresponding value $C_{p,\min}=(2/(\mathrm{Fr}^2\mathrm{Bo})+4\varphi_2(\lambda^2)C_s^2)^{1/2}$. We see that finite elasticity associated with nonzero C_s introduces a correction to the well-known minimum gravity-capillary phase speed $(2/\mathrm{Fr}^2\mathrm{Bo})^{1/2}$ [22,26], and leads to a vertical shift of the curve relative to the classical capillary-gravity case, shown in Fig. 2. However, the minimum still occurs at the same scaled gravity-capillary wave number $K^*=(\rho gL^2/\gamma)^{1/2}$.

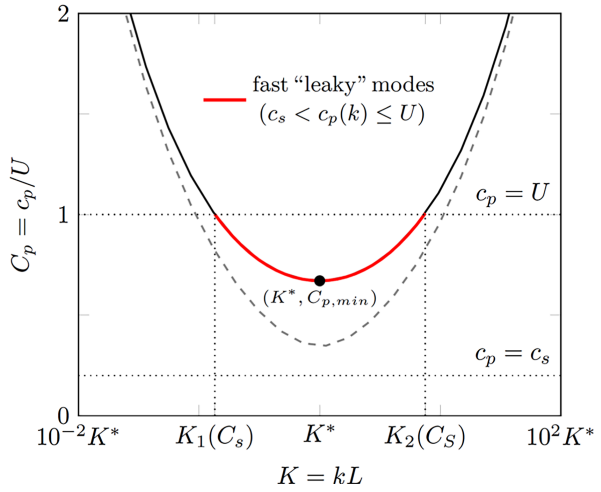

FIG. 2. Dimensionless phase speed C_p of free waves on the surface of an infinitely deep ultrasoft solid with weak elasticity $(C_s\ll 1)$, shown as a function of the scaled wave number K following Eq. (14). The minimum occurs at $K^*=(\rho gL^2/\gamma)^{1/2}$, with a value $C_{p,\min}=(2/(\mathrm{Fr}^2\mathrm{Bo})+4\varphi_2(\lambda^2)C_s^2)^{1/2}$. The dashed line corresponds to the capillary-gravity waves in infinitely deep inviscid liquid without elasticity $(C_s=0)$.

The condition of stationarity that derives from (9) determines the allowable wave numbers for pattern formation, so that setting $C_p=\Omega/K=1$ in Eq. (14) and solving for K gives the critical wave numbers $K_{1,2}(C_s)$. Consequently, wave numbers in the range $K\in[K_1(C_s),K_2(C_s)]$ contribute to constructive interference, as shown in Fig. 2. For a given pressure source speed, the range of allowable wave numbers becomes narrower with increasing elasticity, owing to the vertical shift of the curve shown in Fig. 2.

To compare our theory with observations, we perform numerical simulations to compute the far-field surface wave amplitude that develops in response to an applied pressure field using Eq. (8), with the complete dispersion expression corresponding to Eq. (10). We model the pressure source as a radially symmetric Gaussian field of size L moving with uniform velocity $\boldsymbol{U}$ in the x direction: $P_z(\boldsymbol{x},t;U,L)=P_0\exp[-\pi^2(|\boldsymbol{x}-\boldsymbol{U}t|)^2/L^2]$. Introducing dimensionless variables $\boldsymbol{X}:=\boldsymbol{x}/L$, $W:=w/L$, and recalling the earlier scaling $K=kL$, $\Omega=\omega L/U$, the scaled version of the surface elevation in the comoving frame in Eq. (8) is

$$W(\boldsymbol{X})=\lim_{\epsilon\to 0}\frac{1}{(2\pi)^2}\mathrm{Re}\left[\int\int d^2\boldsymbol{K}e^{i\boldsymbol{K}\cdot\boldsymbol{X}}\frac{\Omega_\epsilon^2K\tilde{P}_z^*(K)}{D(K,\Omega_\epsilon)}\right], \tag{15}$$

where D follows from Eq. (10), $\Omega_\epsilon:=\Omega+i\epsilon=\hat{\boldsymbol{U}}\cdot\boldsymbol{K}+i\epsilon$, and $\tilde{P}_z^*(K):=\tilde{P}_z(K)/(\rho gL^3)\propto\exp(-K^2/4\pi^2)$. For the assumed pressure field, we numerically compute $W(\boldsymbol{X})$ using a two-dimensional inverse fast Fourier transform on a fixed square domain (spanning six wavelengths of gravity wave), discretized on an $N\times N=4096^2$ grid, with the regularization $\Omega\to\Omega_\epsilon$, choosing $\epsilon\approx 10^{-2}$ as a compromise between artificial oscillations introduced by small ϵ and exponential decay at large ϵ, respectively (see SM Sec. D [18] for details).

Sweeping over the scaled parameter space (Fr,C_s), keeping Bo fixed allows us to compare the results with our experiments. In Fig. 3, we show the wake patterns characterized by the opening semiangle α of the leading ridge [35] (see Fig. 6 in End Matter for definitions of α and standard wake angle), from two different sets of simulations performed with $\mathrm{Bo}\approx 3.7$. In Fig. 3(a), the scaled shear-wave speed C_s is varied while keeping the Froude number constant. The opening semiangle α increases with increasing elasticity, and the wake distinctly becomes more spatially damped, consistent with both the theoretical predictions and the experimental trend as shown in Figs. 1(b) and 1(c). In Fig. 3(b), we show the effects of the Froude number Fr on wake angle, that can be achieved by changing either the disturbance size L or speed U.

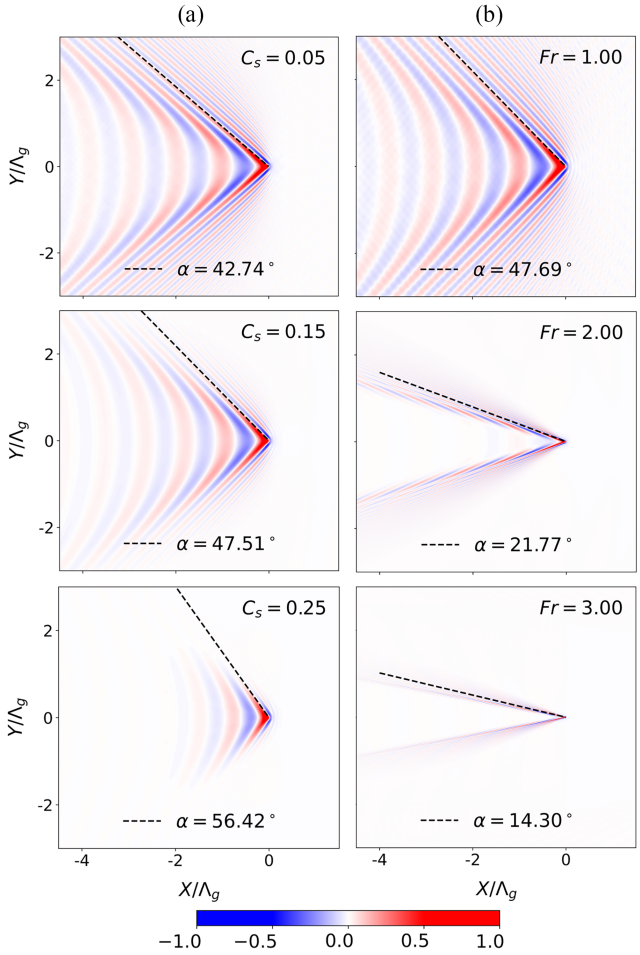

FIG. 3. Wake pattern on ultrasoft solids showing the normalized surface elevation, computed using (15) at Bo ≈ 3.7, for different scaled shear-wave speeds $C_s = c_s/U$ and Froude numbers Fr as functions of the scaled coordinates X/Λ_g and Y/Λ_g, where $\Lambda_g = 2\pi \mathrm{Fr}^2$ is the dimensionless wavelength of the gravity wave corresponding to the source size L. The opening half-angle α of the leading dominant ridge (dashed black line) is shown for increasing (a) C_s at Fr = 1.1 and (b) Fr at $C_s = 0.02$. The computational domain is approximately 0.75 Fr^2 times the length of the experimental tank.

The opening angle decreases at large Fr, in qualitative agreement with our experimental observations in Fig. 1(b).

To quantitatively compare the theory with our experiments, we measure wake opening angles α from simulations for $\mathrm{Fr} \in [1, 3]$ and $C_s \in [0.01, 0.2]$. In Fig. 4 we see that the linear relation obtained using geometric considerations persists, with $\sin\alpha = Ac_s/U$; simulations yield $A \approx 3.5$, while experiments yield $A \approx 4.5$. Similarly, the dependence on Fr follows a Mach-like law, $\sin\alpha = B/\mathrm{Fr}$, with $B \approx 0.91$ from simulations and $B \approx 1.1$ from experiments, showing reasonable agreement. We believe that the primary reason for the difference is finite size effects associated with not being strictly in the deep-water limit.

Our Letter of surface wakes on ultrasoft elastic surfaces uses experiments and theory to probe a previously

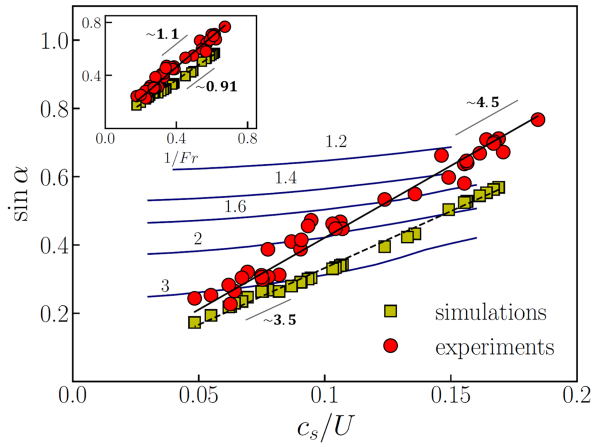

FIG. 4. Plot of $\sin\alpha$ as a function of c_s/U for different Froude numbers Fr, obtained from simulations following (15). Blue curves: iso-Fr contours from simulations, with Fr indicated above each curve. Yellow squares: simulations run at the experimental conditions. Red circles: experimental observations for comparison. The experimental data points that correspond to different pulse speeds U move across iso-Fr curves, such that $\mathrm{Fr}C_s\sqrt{\mathrm{Bo}} = (U/\sqrt{gL})\sqrt{(\mu/\rho U^2)}(\rho g L^2/\gamma)^{1/4} = [(\mu^2/(\rho g\gamma)]^{1/4}$ is constant. The inset shows the wake angle scales with the inverse of Fr, for both experiments and simulations.

unexplored regime where gravity, capillarity, and elastodynamics act together, while bringing together the classical subjects of Rayleigh waves and Kelvin wakes. Our experiments allow us to observe wakes behind a moving source as a function of its speed and our theory shows how the geometric simplicity of Mach-like wakes combines with the dispersive character of gravity-capillary waves. Furthermore, we see that elasticity leads to effective damping through radiative leakage, even in the absence of viscosity. Altogether, our approach also provides a quantitative foundation for probing the dynamics of ultracompliant solid surfaces.

Acknowledgments—This work was supported in part by the Simons Foundation, the Harvard NSF MRSEC 20-11754, and the Henri Seydoux Fund. The computations in this Letter were run on the FASRC FASSE cluster supported by the FAS Division of Science Research Computing Group at Harvard University.

Data availability—The data that support the findings of this article are openly available at [36].

[1] S. Mora, T. Phou, J.-M. Fromental, and Y. Pomeau, Phys. Rev. Lett. **113**, 178301 (2014).
[2] S. Mora, T. Phou, J.-M. Fromental, L. Pismen, and Y. Pomeau, Phys. Rev. Lett. **105**, 214301 (2010).
[3] A. Chakrabarti and M. K. Chaudhury, Langmuir **29**, 6926 (2013).
[4] A. Chakrabarti, M. K. Chaudhury, S. Mora, and Y. Pomeau, Phys. Rev. X **6**, 041066 (2016).

[5] J. F. Greenleaf, M. Fatemi, and M. Insana, Annu. Rev. Biomed. Eng. **5**, 57 (2003).
[6] P. Chantelot, L. Domino, and A. Eddi, Phys. Rev. E **101**, 032609 (2020).
[7] N. Xue, L. A. Wilen, R. W. Style, and E. R. Dufresne, Soft Matter **21**, 209 (2025).
[8] P.-K. Choi, Jpn. J. Appl. Phys. **31**, 54 (1992).
[9] Y. Onodera and P.-K. Choi, J. Acoust. Soc. Am. **104**, 3358 (1998).
[10] X. Shao, J. R. Saylor, and J. B. Bostwick, Soft Matter **14**, 7347 (2018).
[11] J.-C. Ono-dit Biot, M. Trejo, E. Loukiantcheko, M. Lauch, E. Raphaël, K. Dalnoki-Veress, and T. Salez, Phys. Rev. Fluids **4**, 014808 (2019).
[12] J. Bercoff, M. Tanter, and M. Fink, IEEE Trans. Ultrason. Ferroelectr. Freq. Control **51**, 396 (2004).
[13] X. Jacob, S. Catheline, J.-L. Gennisson, C. Barrière, D. Royer, and M. Fink, J. Acoust. Soc. Am. **122**, 1917 (2007).
[14] A. Chakrabarti and M. K. Chaudhury, Extreme Mech. Lett. **1**, 47 (2014).
[15] J. Harden, H. Pleiner, and P. Pincus, J. Chem. Phys. **94**, 5208 (1991).
[16] L. Rayleigh, Proc. London Math. Soc. **s1-17**, 4 (1885).
[17] W. Thomson, Proc. - Inst. Mech. Eng. **38**, 409 (1887).
[18] See Supplemental Material at http://link.aps.org/supplemental/10.1103/lvvp-8pll for movies, additional details on experiments, derivations, and numerical methods, which includes Refs. [19–21].
[19] S. Hassan, J. Kim, and Z. suo, J. Mech. Phys. Solids **158**, 104675 (2022).
[20] Y. Hu and Z. Suo, Acta Mech. Solida Sin. **25**, 441 (2012).
[21] S. I. Tamim and J. B. Bostwick, npj Microgravity **7**, 42 (2021).
[22] H. Lamb, *Hydrodynamics*, 6th ed. (Cambridge University Press, Cambridge, England, 1932).
[23] J. Lighthill, *Waves in Fluids* (Cambridge University Press, Cambridge, England, 1978).
[24] M. Rabaud and F. Moisy, Phys. Rev. Lett. **110**, 214503 (2013).
[25] R. Pethiyagoda, T. J. Moroney, C. J. Lustri, and S. W. McCue, J. Fluid Mech. **915**, A126 (2021).
[26] F. Moisy and M. Rabaud, Phys. Rev. E **90**, 023009 (2014).
[27] In the case of nondispersive Rayleigh waves, we expect $A = 1$.
[28] T. H. Havelock, Proc. R. Soc. A **81**, 398 (1908).
[29] I. Carusotto and G. Rousseaux, *Analogue Gravity Phenomenology: Analogue Spacetimes and Horizons, from Theory to Experiment* (Springer International Publishing, Cham, 2013), pp. 109–144.
[30] See also SM B.1 [18] for a simple scaling derivation of the dispersion relation in the limit relevant for our experiments.
[31] L. D. Landau and E. M. Lifshitz, *Fluid Mechanics*, Course of Theoretical Physics Vol. 6 (Butterworth-Heinemann, London, 1987).
[32] Setting $y = \Omega^2/K^2C_s^2$ we can rewrite this relation as $y(y^3 - 8y^2 + 24y - 16) = 0$, with a single non-trivial real root $y \approx 0.912$, i.e. $\Omega/(KC_s) \approx 0.955$.
[33] For comparison, a solid with much larger modulus, say $\mu \gg 10^2\ Pa$, or low surface tension, can support both fast and slow modes.
[34] The corresponding dimensional version is $\omega = \sqrt{\omega_{cg}^2 + 4\varphi_2(\lambda^2)c_s^2k^2}$, where $\omega_{cg}^2 = gk + \gamma k^3/\rho$ (see SM B.1 [18] for a simple scaling derivation of this relation).
[35] The half-angle α defines the leading dominant ridge, which was visible and measured in the experiments; this is distinct from the wake angle based on β given by Eq. (A2), but that was hard to observe.
[36] A. Chakrabarti, D. Jaganathan, R. Haussman, and L. Mahadevan, Supporting data at 10.7910/DVN/R3I4FZ.
[37] F. S. Crawford, Am. J. Phys. **52**, 782 (1984).

End Matter

Radiation and wake angles—To characterize the nature and form of the wake, we examine the group speed of the wave packets generated by the dispersive system (13), since it determines where the energy of the generated waves focuses spatially. The scaled group speed, $C_g = c_g/U$, corresponding to Eq. (13), is

$$C_g(K) := \frac{\partial\Omega}{\partial K} = \frac{1 + 3K^2/\mathrm{Bo}^2 + 8\varphi_2(\lambda^2)\mathrm{Fr}^2C_s^2K}{2\mathrm{Fr}^2\Omega}. \quad \text{(A1)}$$

In Fig. 5(a), we plot C_g and the phase speed $C_p = \Omega/K$ as a function of K. Just as for classical gravity-capillary waves, there are two distinct branches: waves with $K \in [K_1(C_s), K^*]$ lie on the *elastogravity branch*, where $C_g < C_p$, characteristic of gravity waves, and those with $K \in [K^*, K_2(C_s)]$ lie on the *elastocapillary branch*, where $C_g > C_p$, analogous to capillary waves.

In Fig. 5(b), we show the geometry of monochromatic waves associated with a single wave number generated by the moving source. As it moves from S_{-t} to S_0, where t denotes the elapsed time, circular wave fronts emanate from successive source locations on the horizontal axis. Waves generated earliest at $-t$ travel the farthest at the phase speed c_p, and their constructive interference with the waves generated subsequently produces focusing of wave amplitudes along a particular line. For each admissible wave number in the range $[K_1(C_s), K_2(C_s)]$, this line is characterized by the radiation angle $\beta(K)$ between the source velocity vector $(-\boldsymbol{U})$ and the group velocity vector of the wave packet in the moving frame $(c_g\hat{\boldsymbol{k}} - \boldsymbol{U})$. Following the geometric constructions in [26,37], and considering the magnitudes and directions of the stationary phase [17], the radiation angle of the wave group of a given K is

$$\tan\beta(K) = \frac{C_\mathrm{g}(K)\sqrt{1 - C_\mathrm{p}^2(K)}}{1 - C_\mathrm{g}(K)C_\mathrm{p}(K)}. \quad \text{(A2)}$$

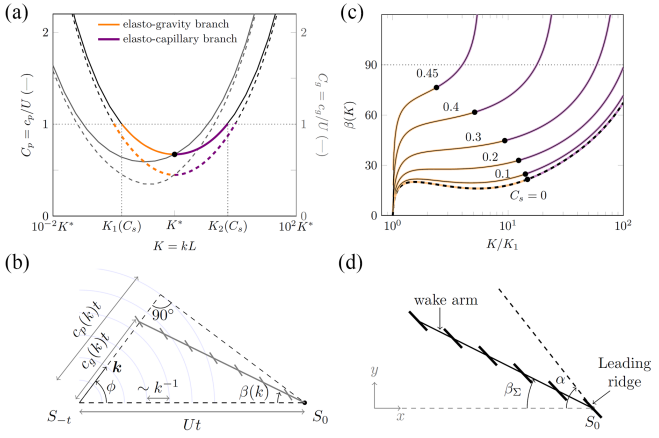

FIG. 5. (a) Dimensionless phase and group speeds as functions of wave number from gravity-capillary elastodynamics ($C_s > 0$) following (14) and (A1), showing the *elastogravity* ($C_g < C_p$) and *elastocapillary* branches ($C_g > C_p$). (b) Schematic of the stationary wake pattern from interference of monochromatic waves generated by a source moving from S_{-t} to S_0, adapted from [26,37]. (c) Radiation angle β for allowed wave numbers at fixed Bo, Fr, with varying shear-wave speeds C_s, following (A2). The dashed curves in (a) and (c) correspond to $C_s = 0$. (d) Schematic of the resultant wake pattern formed by superposition of broadband waves, defining the characteristic angles.

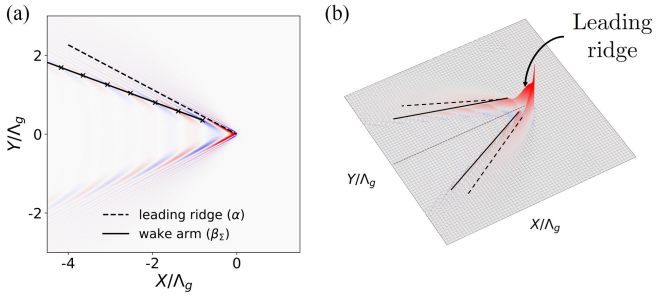

FIG. 6. (a) Top and (b) 3D views of the surface wake pattern for a representative case (Fr $= 1.5$, Bo $= 3.7$, $C_s = 0.01$), showing the difference between the leading dominant ridge (dashed), characterized by the opening angle α, and the wake arm (solid), characterized by the wake angle β_Σ. The markers (×) in (a) indicate the local extremum of the surface displacement field in *each* ridge, and the connecting line passes through these extrema across the successive ridges.

We plot $\beta(K)$ in Fig. 5(c) for different shear-wave speeds by varying C_s. Unlike pure gravity waves in deep water where the wake arm is bounded at the classical Kelvin angle, the radiation angle of free waves on ultrasoft solid spans all directions, similar to gravity-capillary waves. Wave numbers on the elastogravity branch radiate behind source ($\beta < 90^o$), whereas those on the elastocapillary branch radiate in arbitrary directions including ahead of the source ($\beta > 90^o$). Increasing elasticity increases the radiation angle of every allowable wave number. However, the larger wave numbers, which radiate at larger angles, are strongly damped due to elasticity, and thus appear less prominently in the wake pattern.

The constructive interference of the individual wave packets of different wave numbers, each radiating in different angles $\beta(K)$, generates the wake pattern with multiple ridges behind the source [see Fig. 5(d)]. The elevation peaks along these ridges determine the observed wake angle β_Σ, which is different from the opening angle of the leading dominant ridge α. This distinction is shown for a representative set of parameters in Fig. 6. We note that spatial damping due to elasticity makes the observation and measurement of β_Σ in the experiments increasingly difficult for larger C_s, thus driving our choice to measure α rather than the entire wake pattern.